Voltage-controlled spin precession

A. N. M. Zainuddin,* S. Hong, L. Siddiqui, S. Srinivasan, and S. Datta†
School of Electrical and Computer Engineering, Purdue University, West Lafayette, Indiana 47907, USA
(Received 20 July 2010; revised manuscript received 20 February 2011; published 4 October 2011)

Spin-transport properties of a lateral spin-valve structure originating from spin precession in its two-dimensional semiconducting channel under the influence of Rashba spin-orbit (RSO) coupling are explored. The effect of the finite extent of the injecting and detecting contact pads, along the length of the channel, on the spin signals is studied in these structures using (1) a simple theoretical treatment leading to analytical expressions for spin-dependent voltages derived using the stationary phase approximation, and (2) a more rigorous theoretical treatment based on nonequilibrium Green's function formalism to calculate these voltages, in a nonlocal spin-valve setup. Using both these approaches, it is found that the oscillation in spin voltages, which is observed by varying RSO when the magnetization directions of the injector and detector are parallel to the current flow, reduces in amplitude and shifts in phase for contact pads having finite length when compared to the corresponding results for a zero length (point-contact) limit. The amplitude and phase of the oscillation can be recovered to its point-contact limit if the RSO underneath the contacts is assumed to be zero. These models were compared against a recent experiment, and it is found that certain aspects of the experiment can be described well while some other aspects deserve further investigation. Factors that could have influenced the experiment and thereby could explain the discrepancy with the theory were analyzed. Conditions for observing Hanle oscillation in such a structure is discussed. Finally, the possibility of controlling the magnetization reversal via the gate is discussed, which could extend and quantify the 'Datta-Das' effect for voltage controlled spin-precession.

DOI: 10.1103/PhysRevB.84.165306 PACS number(s): 85.75.−d

I. INTRODUCTION

Voltage-controlled spin precession, proposed in 1990,[1] posed two difficult challenges: (1) spin-polarized injection into a semiconducting channel and (2) gate control of the Rashba spin-orbit (RSO) interaction in the channel.[2] The latter was demonstrated by Nitta *et al*. in 1997 using an inverted InGaAs/InAlAs quantum well with a top gate.[3] But spin-polarized injection into a semiconductor proved to be a more difficult challenge[4] which has only recently been overcome through the combined efforts of many groups around the world.[5–8] Very recently, Koo *et al*.[9] combined both ingredients, spin-polarized injection and gate-controlled RSO, into a single experimental structure using a high-mobility InAs heterostructure with a top gate interposed between the current contacts and the voltage contacts. The nonlocal voltage signal[10] shows an oscillatory behavior when the contacts are magnetized along the direction of current flow, but shows nonoscillatory behavior when they are magnetized perpendicular to the current flow, as expected from the theory presented in Ref. 1. Furthermore, it was shown[9] that the oscillation is described well by a single cosine function with an additional phase shift. The oscillation period was $2m^*\alpha(V_G)L/\hbar^2$, where m^* is the effective mass and $\alpha(V_G)$ is the RSO measured independently from the Shubnikov–de Haas (SDH) beating pattern. For carriers flowing in quasi-two-dimensional channels such periodic oscillation is believed to be washed out with increasing number of channels due to the nontrivial intersubband coupling effect.[11–16] However, Pala *et al*.[17] and recently Agnihotri *et al*.[18] showed that for two-dimensional channels of semi-infinite width where periodic boundary conditions (PBCs) can be imposed instead of hard wall boundary conditions (HBCs) along the width direction, such periodic oscillation can still persist although it decays due to the averaging effect over an angular spectrum with increasing strength of the RSO interaction. Based on this observation it would seem that the single cosine-like oscillation observed in Ref. 9 is plausible, but the amplitude and phase require a more detailed consideration especially since the simple models view the contacts as point sources.

The objective of this paper is to first explore the influence of extended injecting and detecting contacts on RSO-modulated spin signals. The model is then compared against the recent experiment[9] and possible sources of discrepancies are discussed. We also discuss the possibility of controlling the magnetization switching via modulating spin-current. We hope that our analysis will establish this gate-controlled spin-precession effect on a firm footing, so that it can be used both for fundamental studies as well as for various proposed applications such as spin filtering, magnetic recording and sensing, or quantum computing.[19]

The organization of this paper is as follows. In Sec. II we provide an overview of our model for calculating spin-dependent voltages in a two-dimensional channel with a RSO. Here we will first provide a simple analytical model which is an extension of the approach taken in Ref. 1 to include the sum over the angular spectrum of electrons. The simple model is followed by a more rigorous nonequilibrium Green's function (NEGF)-based model for electronic transport, with which we simulate an actual nonlocal spin-valve structure. In Sec. III, we discuss spin voltages in the limit of injecting and detecting point contacts. Then in Sec. IV we discuss how the spin voltage reduces in amplitude and changes in shape with the influence of extended contacts. In Sec. V we compare our model with the experiment in Ref. 9, and we discuss possible reasons for discrepancies in Sec. VI. We briefly discuss the magnetic-field-controlled oscillation, Hanle effect, in such RSO-coupled channels in Sec. VII. In Sec. VIII we discuss a scheme to

manipulate the magnetization direction by modulating the gate voltage. Finally, we summarize our conclusions in Sec. IX.

II. MODEL OVERVIEW

We start from an effective mass Hamiltonian for a two-dimensional conductor having a RSO interaction and a negligible Dresselhaus spin-orbit (DSO) interaction of the form ($\vec{\sigma}$: Pauli spin matrices):

$$H = -\frac{\hbar^2}{2m^*}\left(\frac{\partial^2}{\partial x^2}+\frac{\partial^2}{\partial y^2}\right)+\alpha(\sigma_X k_Y - \sigma_Y k_X). \quad (1)$$

A. Simple analytical model

Equation (1) leads to the dispersion relation

$$E = \frac{\hbar^2 k^2}{2m^*} \pm \alpha k, \quad k = +\sqrt{k_X^2+k_Y^2}, \quad (2)$$

with the upper and lower signs corresponding to eigenspinors of the form $\{\psi_\pm\} = \{1 \pm \exp(i\phi)\}^T$, where $\tan\phi \equiv -k_X/k_Y$. Here, X and Y are the longitudinal (or transport) and transverse direction, respectively, following the coordinate system used in Ref. 9, which is different from that used in Ref. 1. Assuming periodic boundary conditions in the transverse direction leads to k_Y being conserved in the absence of any scattering mechanism and also to two values of k_X (k_{X+} and k_{X-}) corresponding to the upper and the lower signs in Eq. (2), which are given by

$$\begin{aligned} E &= \frac{\hbar^2}{2m^*}\left(k_{X+}^2+k_Y^2\right)+\alpha\sqrt{k_{X+}^2+k_Y^2} \\ &= \frac{\hbar^2}{2m^*}\left(k_{X-}^2+k_Y^2\right)-\alpha\sqrt{k_{X-}^2+k_Y^2}, \end{aligned} \quad (3)$$

and for small α we can write

$$k_{X-} - k_{X+} \approx \frac{2m^*\alpha}{\hbar^2}\frac{k_0}{\sqrt{k_0^2-k_Y^2}}, \quad (4)$$

with $k_0 \equiv \sqrt{2m^*E}/\hbar$. Equation (4) determines the frequency at which the spins would rotate while traveling at a certain k_Y mode. It also suggests that the frequency of rotation would be higher for higher k_Y modes. A similar expression for a one-dimensional channel was derived in Ref. 1 [see Eq. (6)], and one can get the same by simply putting $k_Y = 0$ in Eq. (4).

To get the magnitude and phase of oscillation, we calculate the transmission t for an electron injected from a point-contact injector and detected at a point-contact detector separated by a channel length L. Nonlocal voltages $V_{X(Y)}$ [see Fig. 1(a)], for the magnetizations of $X(Y)$-directed injecting and detecting ferromagnetic contacts being parallel and antiparallel, are proportional to $|t_{xx(yy)}|^2$ and $|t_{x\bar{x}(y\bar{y})}|^2$, respectively, and are, henceforth, denoted by $V_{X(Y),P}$ and $V_{X(Y),AP}$, respectively. In this paper, we present the results in terms of a quantity named "spin voltage," which is denoted by $\Delta V_{X(Y)}$ and is defined as $\Delta V_{X(Y)} = [V_{X(Y),P} - V_{X(Y),AP}]$. These notations are similar to the ones used by Takahashi *et al.*[20] Throughout this paper the analytical expressions for spin voltages will be validated by comparing them with the results from a more rigorous model based on NEGF formalism for electronic transport.

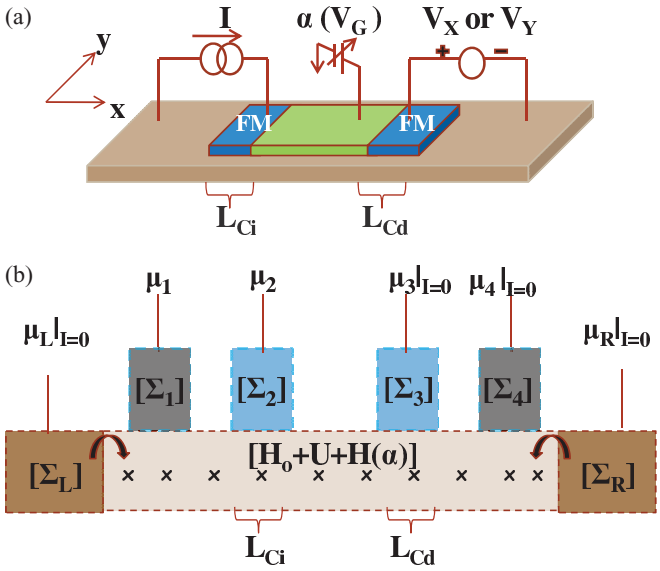

FIG. 1. (Color online) Schematics of (a) a lateral structure under nonlocal setup where V_X (V_Y) corresponds to the spin voltages when the injecting and detecting ferromagnetic (FM) contacts are magnetized in the X (Y) direction, (b) NEGF-based model for the structure in (a) with Σ_2 and Σ_3 representing injecting and detecting FM contacts, Σ_1 and Σ_4 representing nonmagnetic (NM) contacts, and Σ_L and Σ_R representing the semi-infinite regions outside the central region.

B. NEGF-based model

A detailed description of the NEGF-based model can be found in Ref. 21. The inputs to this model are the Hamiltonian [H] and the self-energy matrices [Σ] [Fig. 1(b)]. For H we use a discretized version of the one used in the simple model section [Eq. (1)], described in Ref. 21 assuming PBCs along Y as discussed above. We neglect all scattering processes, assuming both the mean free path and the spin coherence length are longer than the longitudinal dimensions at low temperatures. To understand any signal decay at higher temperatures will require a consideration of both momentum and spin relaxation processes, but we leave this for future work. The self-energies for the ferromagnetic (FM) contacts (Σ_2,Σ_3) have the form $-(i/2)\gamma[I + P_C\vec{\sigma}\cdot\hat{n}]$ where the polarization $P_C = (G_M - G_m)/(G_M + G_m)$ and $\hat{n}$ is the unit vector in the direction of the magnet. Here G_M and G_m are the majority and minority spin-dependent conductances of the tunneling contacts. We note that these spin-dependent interfacial conductances determine the spin accumulation at the ferromagnetic-nonmagnetic interface both in the diffusive and in the ballistic regimes.[22,23] The constant $\gamma = \pi(G_M + G_m)\hbar^3/e^2m^*$ is chosen to give a tunneling conductance equal to the experimental value. The nonmagnetic (NM) contacts (Σ_1,Σ_4) are represented similarly with $P_C = 0$. So G_M and G_m are the only two fitting parameters used in this model. Finally, the long extended regions outside the channel at two ends [see Fig. 1(a)] are represented by two semi-infinite contacts whose coupling is given by $\Sigma_{L(R)} = \tau_{L(R)}g_S\tau_{L(R)}^\dagger$,

where τ is the spin-dependent coupling matrix between the contact and the channel and g_S is the surface Green's function. The transmission functions are calculated from the NEGF model and contacts 3, 4, L, and R are treated as voltage probes with zero current (following the approach introduced by Buttiker, see Sec. 9.4, in Ref. 24). We note that although we are not including any scattering processes explicitly, the voltage probes introduce an effective spin scattering that reduces the signal. This is due to the fact that for the charge current to be zero in a voltage probe, two spin components, majority and minority spins, of the current become equal in magnitude. Thus majority spins convert to minority spins and thereby spin relaxation takes place. To explain further about our method of calculating nonlocal spin voltages, we compare our NEGF-based calculation with an equivalent circuit model in Appendix A for a given structure. The results are consistent with those of the ballistic model of spin signal described in Ref. 23.

In the following sections we discuss the magnitude and phase of spin voltage for the structure shown in Fig. 1(a) featuring the effects of contacts based on both our simple and NEGF-based models.

III. DEVICE WITH POINT CONTACTS

We start our discussion by considering a point-contact injector and a point-contact detector. It is shown in Appendix B that starting from the eigenspinors in Eq. (2) and assuming ballistic transport in the channel, the contributions to the voltage signals for X- and Y-directed magnets coming from a particular E and k_Y can be written as (C_0: constant)

$$\Delta V_{X0}(E,k_Y) = C_0\left\{s^2 + (1-s^2)\cos\left(\frac{\theta_L}{\sqrt{1-s^2}}\right)\right\}, \quad (5a)$$

$$\Delta V_{Y0}(E,k_Y) = C_0\left\{(1-s^2) + s^2\cos\left(\frac{\theta_L}{\sqrt{1-s^2}}\right)\right\}, \quad (5b)$$

where $s \equiv k_Y/k_0 = \hbar k_Y/\sqrt{2m^*E}$ and $\theta_L = 2m^*\alpha L/\hbar^2$. These contributions from different E, k_Y all act "in parallel," giving a voltage equal to the average. At low temperatures we can average the contributions from all transverse wave vectors k_Y over the Fermi circle ($E = E_F$) to write

$$\Delta V_{X(Y)} = \int_{-k_0}^{+k_0} \frac{dk_y}{2\pi k_0}\Delta V_{X0(Y0)}(E_F,k_Y). \quad (6)$$

We note that Eq. (6) is equivalent to the conductance modulation expressions derived in Refs. 17 and 18 for a two-terminal spin field-effect transistor. Interestingly, the results obtained from the integration in Eq. (6) look almost like a single cosine. This can be understood by noting that the argument $\theta_L/\sqrt{1-s^2}$ has a stationary point at $s = 0$,[25] and we can use the method of stationary phase to write approximately

$$\Delta V_X \simeq \frac{C_0}{3\pi} + \frac{C_0}{\sqrt{2\pi\theta_L}}\cos\left(\theta_L + \frac{\pi}{4}\right), \quad (7a)$$

$$\Delta V_Y \simeq \frac{2C_0}{3\pi}. \quad (7b)$$

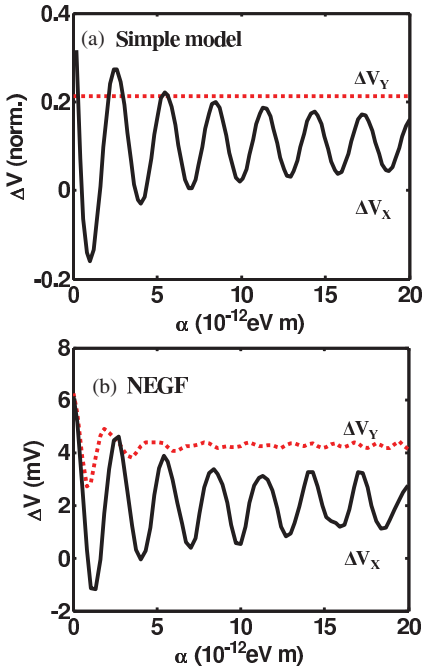

FIG. 2. (Color online) Spin voltages as a function of the RSO for both X- and Y-directed point injecting and detecting ferromagnetic contacts from (a) analytic expression in Eq. (7) for ΔV_Y and ΔV_X, (b) NEGF-based model. Parameters: $P_C \sim 1$ and $n_S = 2.7 \times 10^{12}$ cm^{-2}, and the spacing between two point contacts is 1.65 μm.

As shown in Appendix C these approximations describe the results from the exact integration quite well for $\theta_L \gtrsim 2\pi$ which falls within the current experimental status.[9]

Although the simple model here makes no prediction about the amplitude C_0, it does suggest that the peak-to-peak amplitude of the oscillation in ΔV_X should be $3\pi/\sqrt{2\pi\theta_L}$ times the spin-valve signal ΔV_Y. This is shown in Fig. 2(a) by plotting the analytical expression in Eq. (7) and is also evident from our numerical NEGF-based model as shown in Fig. 2(b).

IV. DEVICE WITH EXTENDED CONTACTS

In this section we consider injection and detection from contacts that are extended over the channel along x. In the point-contact case, all the injected electrons travel across the same length L before reaching the detector. But with extended contacts, electrons will travel across a length depending on the point of injection and the point of detection under the contacts. This will give rise to a spread in the values of θ_L in Eqs. (5a) and (5b). We can write

$$\widetilde{\Delta V}_X = C_i C_d \frac{C_0\cos(\theta_0+\theta_i+\theta_d+\pi/4)}{\sqrt{2\pi(\theta_0+\theta_i+\theta_d)}}, \quad (8)$$

where C_i and C_d are numbers less than unity representing the averaging effects of the injecting and detecting contacts, respectively, and θ_i, θ_d are the additional phase shifts introduced by the injecting and detecting contacts, respectively, in addition to θ_0, which is the phase shift corresponding to the channel length between the contacts. θ_i, θ_d or C_i, C_d will

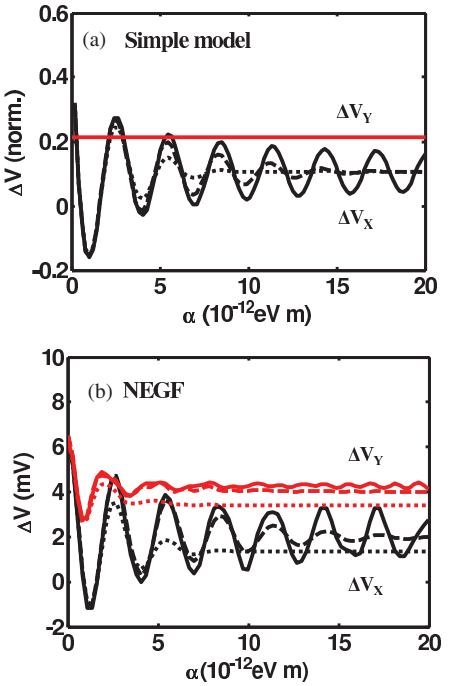

FIG. 3. (Color online) Spin voltages as a function of the RSO for both X- and Y-directed extended contacts with uniform injection and detection. (a) Analytic expression in Eq. (8) for ΔV_X and in Eq. (7b) for ΔV_Y, (b) NEGF-model-based calculation for the same signals. Parameters: same as in Fig. 2 for point contacts (solid), and $L_{C_{i,d}} = 0.2\ \mu$m (dashed) and 0.4 μm (dotted) for extended contacts.

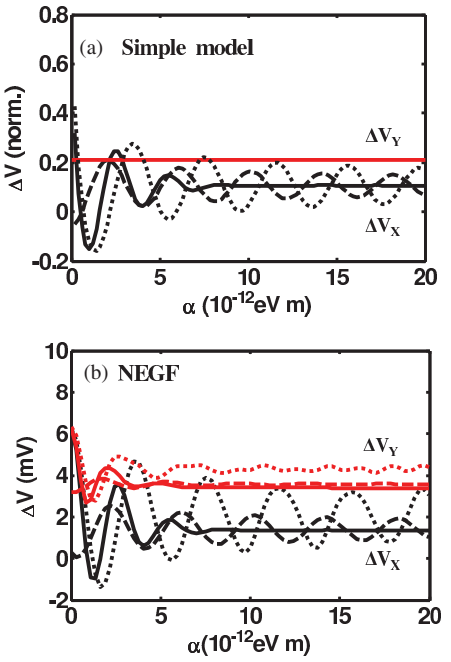

FIG. 4. (Color online) Spin voltages as a function of the RSO for both X- and Y-directed extended contacts where the RSO in the channel under the contacts does not vary in accordance with the channel outside the contacts. (a) Analytic expression in Eq. (8) for ΔV_X and in Eq. (7b) for ΔV_Y, (b) NEGF-model-based calculation, for cases (1) when RSOs under the the contacts vary accordingly with the rest of the channel outside the contacts $\alpha_0 = \alpha$ (solid), (2) RSOs under the contacts are fixed at $\alpha_0 = 4 \times 10^{-12}$ eV m (dashed), and (3) RSO is absent under the contacts $\alpha_0 = 0$ (dotted). Other parameters are the same as in Fig. 3.

depend on (A) the length of the injecting and detecting contacts and (B) how the RSO $\alpha(V_G)$ varies under the contacts. We discuss these two points in the following sections. However, we note that extended contacts do not affect ΔV_Y, because it is nonoscillatory. As a result, ΔV_Y can be described by the same Eq. (7b) even with extended contacts.

A. Length of the contacts

It is shown in Figs. 3(a) and 3(b) that, considering uniform injection and detection along the channel, the oscillatory signal (ΔV_X) reduces in amplitude and shifts in phase with increasing contact lengths. Besides, the fact that the nonoscillatory signal stays almost the same with contact lengths is also verified from the NEGF calculation [see ΔV_Y in Figs. 3(a) and 3(b)]. Here the signal ΔV_X is averaged over both the injecting and detecting contacts for which the amplitude degrades. As a result the ratio $\Delta V_Y/\Delta V_X$ (peak-to-peak or "p-p") is further increased from the point-contact limit. Our analytical result [Eq. (8)] also matches that from the NEGF model if we use $\theta_{i,d} = m^*\alpha L_{C_{i,d}}/\hbar^2$ and $C_{i,d} = \sin(\theta_{i,d})/\theta_{i,d}$ which can be justified if the electronic wave function is assumed to remain constant under each contact.

B. Variation of RSO under the contacts

Since the contacts are metallic, and in addition to being ferromagnetic, it is possible for the gate electric field to be screened out under the contacts. In such a case, the RSO underneath the contacts α_0 might not follow the variation that the gate electric field brings about in the "bare" channel region not placed underneath the contacts. Moreover it is also possible that, underneath the contacts, the local magnetic field reduces the RSO. However, a detailed treatment of this issue is beyond the scope of this paper. Here we only show how various choices of RSOs under the contacts can change the shape and amplitude of the oscillatory ΔV_X. In Fig. 4 (solid line) we find that if RSO varies under the contacts, oscillation is washed out at higher α. However, for a fixed RSO under the contact the situation [see Fig. 4 (dashed)] improves, because now $\theta_{i,d} = 2m^*\alpha_0 L_{C_{i,d}}/\hbar^2$ under the contacts do not vary with the increase in RSO in the channel outside the contacts and hence $C_{i,d} = \sin(\theta_{i,d})/\theta_{i,d}$ has a constant value which was otherwise decreasing with the increase in α_0. In this case the ratio $\Delta V_Y/\Delta V_X$(p-p) reduces with decreasing α_0 and it reaches again the point-contact limit when α_0 is assumed to be zero under the contacts [see Fig. 4 (dotted)].

V. COMPARISON WITH EXPERIMENT

Next we compare our models against the experiment in Ref. 9. To obtain a current level equal to the experimental value in the NEGF model we adjust the applied potential difference $(\mu_1 - \mu_2)$ for contacts 1 and 2 [see Fig. 1(b)]. We use a contact conductance of $G_C = G_M + G_m = 4 \times 10^{10}\ \Omega^{-1}\text{m}^{-2}$ based on the experimental parameters in Ref. 9 and $P_C = (G_M - G_m)/(G_M + G_m) \sim 0.05$ to match the spin-valve signal ΔV_Y.

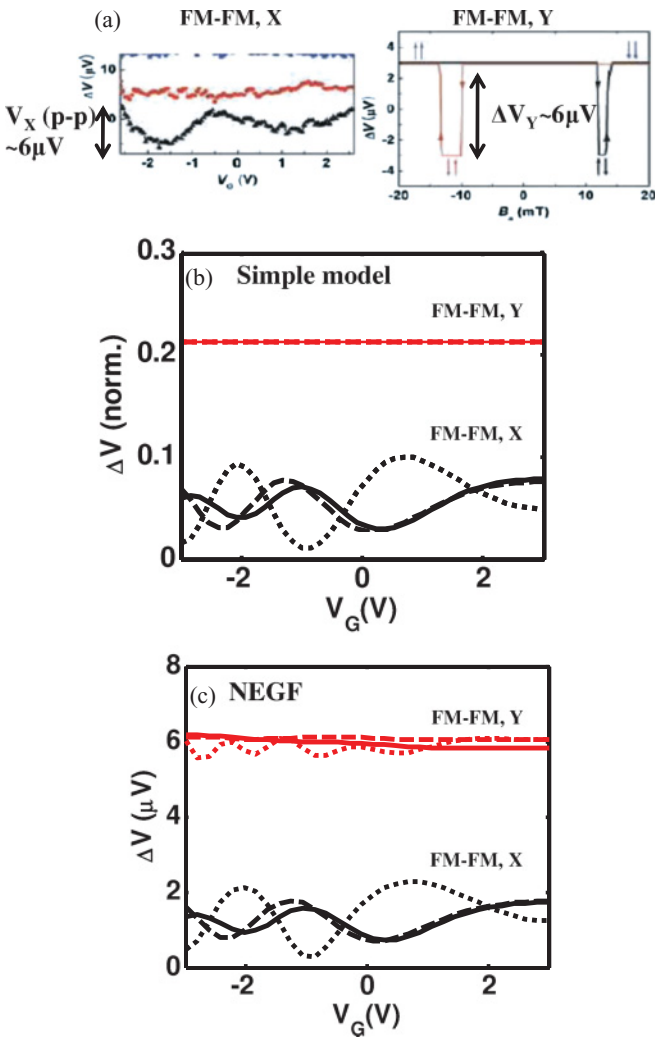

FIG. 5. (Color online) Comparison with experiment in Ref. 9. (a) Experimental observation for nonlocal voltage in X- and Y-directed injector and detector. Reprinted with permission from science publishing group. (b) Simple qualitative model and (c) NEGF model. In all cases RSO under the contacts α_0 is varied among three choices: (1) α_0 varies according to the channel $\alpha(V_G)$ (solid), (2) α_0 is kept fixed at $\alpha(V_G = 0)$ (dashed), and (3) α_0 is assumed zero (dotted). Parameters: $P_C \sim 0.05$, $n_S = 2.7 \times 10^{12}/\text{cm}^2$, $G_C = G_M + G_m = 4 \times 10^{10}\ \Omega^{-1}\text{m}^{-2}$, $L_{C_i} = 0.2\ \mu$m, and $L_{C_d} = 0.25\ \mu$m with 1.65 μm spacing in between.

To be consistent with the notations used in Ref. 9 we relate the measured oscillatory signal $V_{X,P}$(p-p) [Fig. 5(a) left panel] to our calculated oscillatory spin voltage $\Delta V_{X,P}$ a: $V_{X,P}$(p-p) $= \Delta V_X/2$ while the measured nonoscillatory spin-valve signal [Fig. 5(a) right panel] can be directly compared to our calculated spin voltage ΔV_Y. We note that to obtain the right shape of the oscillatory signal $V_{X,P}$, we need to consider the contact length to be half of its actual length with a spacing of 1.65 μm [Figs. 5(b) and 5(c)] between them rather than the full contact length. But most importantly, although we find the peak-to-peak amplitude of the oscillatory signal $V_{X,P}$ (FM-FM,X) is to be equal to the spin-valve signal ΔV_Y (FM-FM,Y) in the experiment [see Fig. 5(a)] we observe a much smaller signal for $V_{X,P}$ compared to ΔV_Y in our calculations [Figs. 5(b)–5(e)]. We obtain the closest agreement with the experimental results when we neglect the contact averaging effect by assuming RSO to be zero under the contacts [Figs. 5(b)–5(e) dotted lines], which leads to the point-contact limit as discussed in Sec. IV B. Such a condition gives the minimum calculated $\Delta V_Y/V_{X,P}$(p-p) which, using $m^* = 0.05m_0$, $\alpha \simeq 10^{-11}$ eV m, and $L = 1.65\ \mu$m, is equal to 2.4, and is apparently larger than the experimentally observed value.

In summary, our models (1) explain the observed period of the nonlocal voltage oscillation, (2) point out the fact that the phase requires a better understanding of α under the contacts and show that a certain (nonunique) choice fits the data, and (3) show that the amplitude is larger than expected.

VI. DISCUSSION

In this section we discuss a few possible sources of discrepancy that could have reduced the ratio $\Delta V_Y/V_{X,P}$(p-p) even below the point-contact limit.

A. Dresselhaus spin-orbit coupling

Although we have neglected DSO (see Sec. II) so far in our calculation, in this section we would like to investigate whether a significant DSO along with RSO could have explained the discrepancy with the experiment. In the experiment, DSO was assumed to be negligible compared to RSO since the material has a narrow band gap.[26,27] However, it was shown later[28,29] that DSO can become comparable to RSO in similar structures. As a result, further investigation of the influence of DSO on RSO-modulated signals revealed that the choice of crystallographic orientation of the channel material plays an important role in the Datta-Das effect.[15,30] So in this work, we also incorporated the effect of DSO by including a linear DSO term with the Hamiltonian H in Eq. (1) to write $H_{\text{dso}} = H + \beta(\sigma_X k_X - \sigma_Y k_Y)$, where β is the linear DSO coefficient. Here we are neglecting the cubic DSO term since it only modifies the linear DSO term.[28] In Fig. 6, we show our NEGF simulation that depicts the influence of DSO on the spin voltages. The results indicate that the ratio $\Delta V_Y/V_{X,P}$(p-p) would have increased more, if the DSO were comparable to RSO in the experiment.

B. Boundary scattering

Next, we discuss the role of boundary scattering on the RSO modulation. In our models we have assumed PBC in the Y direction making k_Y a "good quantum number" like E. But when a real confining potential is used for HBC, simple decoupling of different transverse wave vectors (k_Y) is not allowed due to nontrivial "boundary scattering." In this section our numerical calculation shows that, although for smaller number of transverse modes (in a narrow channel) the results are very different, for larger number of modes (in a wider two-dimensional channel), use of HBC does not change the conclusions described above with PBC in a significant way. We show a comparison of HBC and PBC to calculate $\Delta T = |t_{xx(yy)}|^2 - |t_{x\bar{x}(y\bar{y})}|^2$ for the structure shown in Fig. 1 in the point-contact limit. To include HBC, the Hamiltonian is written as $H_{\text{hbc}} = H + V_C(y)$, where H is the Hamiltonian

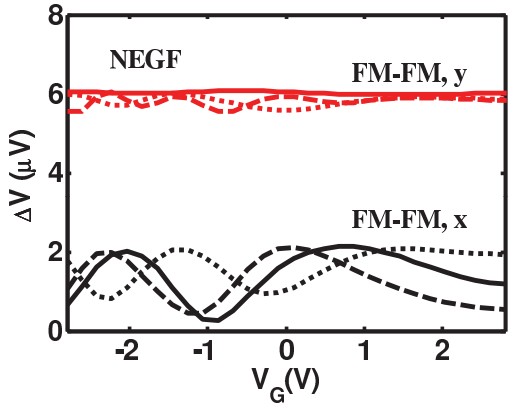

FIG. 6. (Color online) Spin voltages in the presence of DSO coupling, β, in addition to RSO in the point-contact regime. Calculation is done with the NEGF-ased model. Solid lines correspond to spin voltages without DSO ($\beta = 0$), dashed line corresponds to the case when $\beta = 0.2\alpha$ ($V_G = 0$), dotted line corresponds to the case when $\beta = 0.5\alpha$ ($V_G = 0$). Parameters are same as in Fig. 5.

given by Eq. (1) and $V_C(y)$ is a confining potential of the form $V_C(y) = 0$ for $0 < y < W$ and $V_C(y) = \infty$ otherwise. W is the channel width which is varied to include a different number of modes in the channel. Figure 7 shows our two-dimensional real-space NEGF simulation[24] results. We see that for lower number of modes the results are quite different depending on the choice of boundary conditions [see Figs. 7(a) and 7(b)] and indeed for channels with smaller widths, where HBC is more appropriate, RSO-induced oscillation looks non sinusoidal.[11–16] However, with increasing number of modes, HBC and PBC do not show much difference in results [see Figs. 7(c) and 7(d)] suggesting that our PBC-based conclusions (which are in agreement with Refs. 17, 18) should hold quite well for HBC as well.

C. Spin relaxation

In this type of spin orbit material, the dominant spin-relaxation mechanism is believed to be that of the D'yakonov-Perel (DP) type.[31,32] The effect of such a relaxation mechanism has been extensively studied in disordered two-dimensional electron gas (2DEG) under a quantum transport approach (see, for example, Refs. 11, 33–35). But generally spin-orbit interaction effects in spin transport are taken into account in a semiclassical approach[26,36] through their role in relaxing the nonequilibrium spin polarization. The spin-relaxation length of the channel is then obtained from this approach. In the present experiment, the spin-relaxation length λ_{sf} and the mean free path λ_m were found to be $\sim 2\ \mu$m[37] and $\sim 1.61 \pm 0.23\ \mu\text{m}\,(T = 1.8K)$,[9] respectively. But the channel length (length between the injector and detector) of 1.65 μm was found to be shorter than both λ_{sf} and λ_m.[9] As a result, we believe, the DP spin-relaxation mechanism should not change our conclusions in any significant way as well. However, it is quite possible that high k_Y components are suppressed because they actually travel a longer length compared to the lower ones and hence have shorter effective spin coherence lengths which is not considered in a purely ballistic theory. As a result,

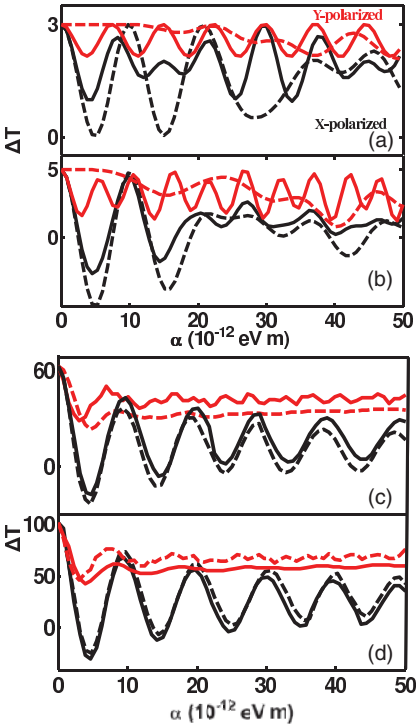

FIG. 7. (Color online) $\Delta T = |t_{xx(yy)}|^2 - |t_{x\bar{x}(y\bar{y})}|^2$ as a function of RSO for different choices of boundary conditions with various numbers of conducting channels. Solid and dashed lines correspond to the results for periodic and hard-wall boundary conditions imposed along the width (Y) direction, respectively. Red and black lines correspond to the results for the magnets directed along Y and X directions, respectively. The number of conducting channels are increased from panels (a)–(d) by varying the width of the channel. Parameters: $n_S = 1 \times 10^{12}$ cm^{-2}, $L_{\text{ch}} = 0.5\ \mu$m, $P_C \sim 1$.

we have included the effect of the spin-relaxation process phenomenologically through an exponential decay function with respect to the value of λ_{sf}. We found that the difference in magnitude of $V_{X,P}$(p-p) and ΔV_Y reduces with shorter λ_{sf}. This is because high k_Y modes relax faster than the low k_Y modes which would reduce the angular averaging effect and the signal would become more and more one dimensional. However, even there we found, assuming point contact, that a reasonable agreement with the experiment requires a spin coherence length much smaller than the value mentioned in the experiment. The details are explained in Appendix D.

Another possibility for the discrepancy is that the P_C we use was calibrated for the spin-valve signals obtained with Y-directed magnets. The same magnets when forced into the X direction for the oscillatory signals may have a higher effective P_C. However, to account fully for the discrepancy we needed to increase the P_C value to $\sim 10\%$ for X-directed magnets while keeping $\sim 5\%$ for the Y-directed magnets.

VII. SPIN PRECESSION IN MAGNETIC FIELD

An important question to address would be whether it is possible to control the precession of spins, in an RSO-coupled ballistic channel like the one in Ref. 9, with a magnetic field of magnitude similar to the values used in observing Hanle

signals in a diffusive channel having no RSO interaction. Typically Hanle signals are measured by applying a magnetic field of a few hundred Gauss perpendicular to the direction of the injected spin direction. For example, when the injected spins are either X or Y polarized in the x-y transport plane, a magnetic field B_z, applied in the z direction, will create a spin precession and generate Hanle voltage at the detector. An expression for the Hanle voltage due to varying B_z, similar to the one due to varying RSO, for the structure shown in Fig. 1(a) can be obtained by including the $\frac{1}{2}g\mu_B B_z$ term in the Hamiltonian in Eq. (1) and following a derivation procedure similar to that in Appendixes B and C, which finally gives

$$\Delta V_X \simeq \frac{aC_0}{3\pi} + \frac{C_0}{\sqrt{2\pi\theta_L^{B_z}}}\cos\left(\theta_L^{B_z} + \frac{\pi}{4}\right), \tag{9a}$$

$$\Delta V_Y \simeq \frac{2aC_0}{3\pi} + \frac{bC_0}{\sqrt{2\pi\theta_L^{B_z}}}\cos\left(\theta_L^{B_z} + \frac{\pi}{4}\right), \tag{9b}$$

where

$$\theta_L^{B_z} \approx \frac{2m^*}{\hbar^2 k_0}\sqrt{(\alpha k_0)^2 + \left(\frac{1}{2}g\mu_B B_z\right)^2}\,L,$$

$$a = \frac{4c_{B_z}^2}{\left(1+c_{B_z}^2\right)^2}, \quad b = \frac{\left(1-c_{B_z}^2\right)^2}{(1+c_{B_z}^2)^2},$$

$$c_{B_z} = \frac{\alpha k_0}{\frac{1}{2}g\mu_B B_z + \sqrt{\left(\frac{1}{2}g\mu_B B_z\right)^2 + (\alpha k_0)^2}}.$$

Here the effect of the vector magnetic potential is neglected, which limits our analysis to small magnetic fields far from the quantum Hall effect regime.

In a ballistic channel, similar to that in a diffusive channel, the oscillatory Hanle signal decays with an increasing B_z due to a spread in transit times of electrons, although the origin of such spread in the former is not the same as it is in the latter. In a diffusive channel the mentioned spread originates from the differences in transit times corresponding to different random-walk trajectories taken by the electrons while going from the injector to the detector. In a ballistic channel it would be the differences in transit times corresponding to different electronic transverse modes that would give rise to such spread. The consequent decay in the Hanle signal for an increasing magnetic field in a ballistic channel appears quantitatively through the dependence of the quantity $\theta_L^{B_z}$, in the modulating prefactor of the oscillating terms in Eqs. (9a) and (9b), on B_z. At the same time its dependence on RSO strength α, in addition to its dependence on B_z, suggests that B_z needs to be larger in a material having strong α [such as an InAs quantum well (QW), where $\alpha \sim 8\times10^{-12}$ eV m] than that in a material having weak α to create any significant change in $\theta_L^{B_z}$ leading to a significant decay in the Hanle signal. Such a scenario can be interpreted in terms of an internal magnetic field $B_{\mathrm{RSO}} = 2\alpha k_0/g\mu_B$ due to RSO, which acts in addition to B_z. This observation suggests that for B_z to have any effect on the Hanle signal its magnitude needs to be comparable to B_{RSO}. In the case of an InAs QW, for $k_0 \sim 4\times10^8$ m^{-1} (corresponding to a carrier density $n_s = 2.7\times10^{12}$ cm^{-2}) and $|g| = 15$,[9] $B_{\mathrm{RSO}} \sim 8$ T, which necessitates the exertion of a very large B_z that might even take the material into a quantum Hall regime. However, by tuning α[38,39] and n_s, the magnitude of B_{RSO} and, hence, the required B_z can be made smaller. Indeed, it would be interesting to look for a Hanle signal as well as a RSO-modulated signal in the same structure where α can be tuned through ~ 0 to a higher value. In that case, one has to be careful about choosing the parameters to observe Hanle oscillation near $\alpha \sim 0$. For example, to rotate the spins by 2π within a ballistic channel length of $L \sim 4$ μm, which can be obtained in InAs 2DEG samples,[40] and a carrier density of $\sim 10^{11}$ cm^{-2}, $g\mu_B B_z$ has to be varied from 0 to 0.2 meV. On the other hand, to get a similar 2π rotation by varying RSO with the same parameters, α needs to be varied from 0 to 1×10^{-12} eV m.

VIII. VOLTAGE-CONTROLLED MAGNETIZATION REVERSAL

Finally, we discuss the possibility of controlling magnetization reversal by modulating spin-current[41] (I_s), which could be an alternative way to demonstrate voltage controlled spin-precession effect. Recently, in lateral structures with metallic channels, spin-torque[42,43] induced magnetization reversal has been demonstrated by pure spin-current.[44,45] Similar switching mechanism is yet to be seen in semiconductor lateral structures, although spin-torque switching is already seen in semiconductor vertical structures (magnetic tunnel junctions).[46,47] Moreover, spin-orbit coupling effect in spin-torque is a relatively new area where conventional spin-torque theories are extended to include spin-orbit coupling inside the ferromagnet[48–50] and a few experiments[51,52] seem to show this. Here we discuss how one might design experiments involving channels with strong spin orbit coupling. Gate control over such channels would allow modulation of the RSO coupling coefficient which in turn would modulate the magnitude and direction of I_s in the channel. Reversing the sign of I_s in the channel could in principle allow for reversible switching of magnetization of a magnet on which this I_s is exerting a torque.

In Fig. 8 we are showing different components of I_s in x, y, and z directions for each of the three different magnet configurations, namely, FM-FM, x, FM-FM, y, and FM-FM, z. They are calculated within our NEGF based model using the generalized current operator described in Ref. 53. We provide the equation in Appendix E. The variation of spin-current components with α implies that the spin-torque exerted on the detecting magnet can be controlled, and thereby a switching event, with a gate. Moreover, since any component of I_s which is perpendicular to the direction of magnetization is going to exert a torque on the magnet, it might also be possible to switch the magnet in a desired direction with a careful tuning of α. The magnitude of I_s can be estimated from the equivalent circuit model shown in Appendix A, which is $I_s = \frac{\Delta V}{P_C}\frac{2G_M G_m}{G_M+G_m}$ (per unit area), for the magnets in collinear configuration. Here ΔV is the spin-valve voltage ($V_P - V_{AP}$). P_C and $G_{M(m)}$ are related to the interface of the magnet to be switched. We also provide a comparison of I_s calculated from this expression against the same with that of the NEGF based model for various P_C and $G_C = G_M + G_m$ values in Appendix E, for further clarification.

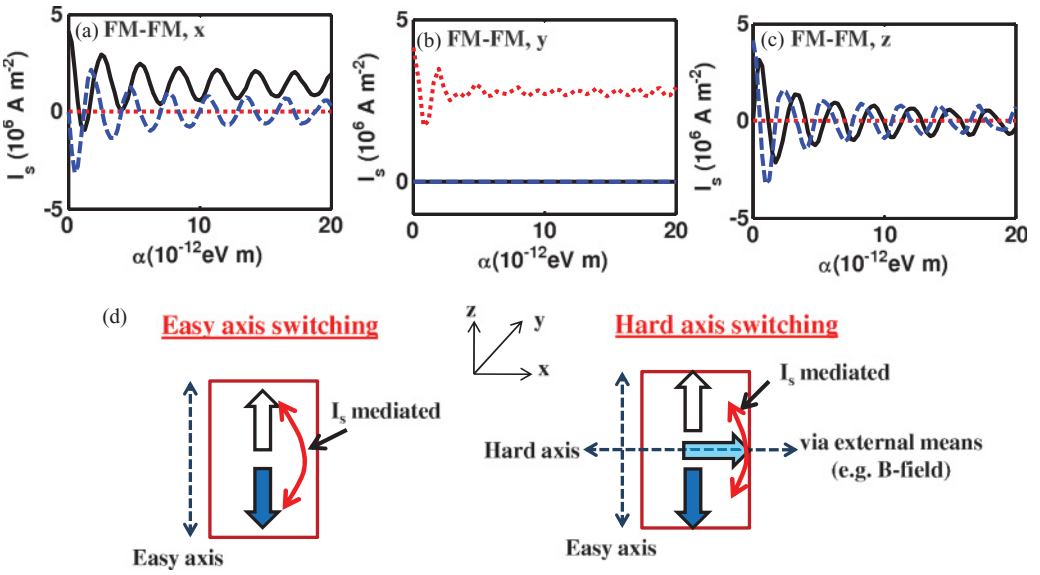

FIG. 8. (Color online) (top) Spin-current components in x (solid black), y (dotted red), and z (dashed blue) directions with RSO calculated from the NEGF based model for magnets along x (FM-FM, x) (a) y (FM-FM, y) (b) and z (FM-FM, z) (c) directions. Parameters: $L_{ch} = 1.65\ \mu$m, $L_{Ci} = 0.2\ \mu$m, $L_{Cd} = 0.25\ \mu$m, $W = 8\ \mu$m, $P_C \sim 5\%$ and $G_M + G_m = 4 \times 10^{10}\ \Omega^{-1}\text{m}^{-2}$. Charge current is maintained at 1 mA. (bottom) Different switching mechanisms are shown schematically in (d).

Considering the spin-valve structure in Ref. 9, the I_s at the detecting magnet would be $\sim 2.4 \times 10^6\ \text{Am}^{-2}$, for $\Delta V \sim 6\,\mu\text{V}, P_C \sim 5\%$ and $(G_M + G_m) \sim 4 \times 10^{10}\ \Omega^{-1}\text{m}^{-2}$. This value of I_s, at present, would be few orders of magnitude smaller than those of metal based structures, for example the structure in Ref. 44, mainly due to the smaller number of conducting modes and spin-polarization in semiconductors than in metals. As a result, if I_s is insufficient to switch a regular magnet, one could consider magnetic semiconductors since a lower switching current was reported in Refs. 46, 47 for the latter compared to a regular magnet. But, in general, if I_s is lower than the critical limit for easy-axis switching [Fig. 8(d), left], which is usually believed to be given by Eq. 18 in Ref. 41 for monodomain magnets, one could also use hard-axis switching [Fig. 8(d), right]. A possible scheme could be to follow a two step process similar to the one introduced by Benett.[54] In the first step, the magnet is taken into its hard axis through an external means (e.g., B-field), where it is unstable, and in the next step a small tilt due to the I_s induced spin-torque will tip the magnet to one of its easy axes once the external field is removed. This idea of two step switching process is also being used in various contexts.[51,55,56] But here also the I_s induced torque has to overcome the thermal noise which depends on the temperature of operation[57] along with other few nonideal factors (see the Supplementary Information in Ref. 56 for a detailed analysis of hard axis switching).

IX. CONCLUSION

In summary, we have studied spin transport through a channel with RSO coupling. We provide both a simple analytical model as well as an NEGF-based model to calculate the spin voltages in a nonlocal spin-valve structure. We discuss the effect of having extended contacts in addition to the effect of angular spectrum averaging of electrons flowing in a two-dimensional channel. The extended nature of the contacts is found to be detrimental to the oscillatory behavior of spin signals. The model is used to analyze a recent experiment[9] and, the results are summarized in Sec. V in addition, the Hanle oscillation in the presence of RSO is also discussed. Finally, the possibility for gate controlled switching of magnetization through spin-current modulation is discussed which could extend and quantify the 'Datta-Das' effect for voltage controlled spin-precession.

ACKNOWLEDGMENTS

This work is supported by the Office of Naval Research under Grant No. N0014-06-1-2005 and the Network for Computational Nanotechnology (NCN). Also ANMZ would like to thank Angik Sarkar and Behtash-behinein for helpful discussions.

APPENDIX A: NONLOCAL VOLTAGE

In this section we explain the nonlocal voltage calculated using an NEGF-based approach with a simple circuit model. As mentioned earlier that the contacts are adjusted to fit the experimental contact conductances, an equivalent conductance network can be drawn for the structure shown in Fig. 1(b) [see Fig. 9(a)]. Here the spin-dependent contact conductances are connected to their respective spin-dependent channels for two spins in the semiconducting 2DEG. The semi-infinite leads $\Sigma_{L(R)}$ at two ends connect the two spin channels and thereby act as a spin-flip conductance of $(q^2/h)M$ each. In Fig. 9(b) we show the nonlocal voltage $\Delta V = [\mu_{3P} - \mu_{3AP}]/q$ from the

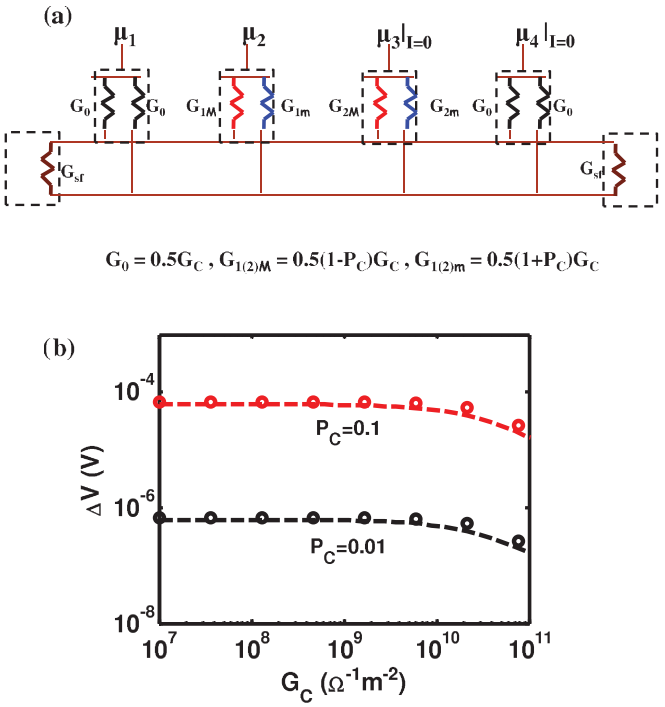

FIG. 9. (Color online) (a) Simple circuit model to illustrate the method of calculating nonlocal voltage in the spin-valve setup in NEGF, (b) nonlocal voltage ΔV calculated from the simple circuit model (solid lines) in (a) compared against the same from the NEGF-based model (circles) as a function of contact conductance $G_C = (G_M + G_m)\ \Omega^{-1}\mathrm{m}^{-2}$ and P_C. Parameters: $L_{C_i} = 0.2\ \mu$m, $L_{C_i} = 0.25\ \mu$m, separation between the contacts 1.65 μm, carrier density $n_S = 2.7 \times 10^{12}\ \mathrm{cm}^{-2}$.

NEGF model compared against the simple circuit model as a function of contact conductance $G_C = (G_M + G_m)\ \Omega^{-1}\ \mathrm{m}^{-2}$ for different contact polarization P_C. In all cases we maintained a current of 1 mA between contacts 1 and 2. We see that the simple circuit agrees well with the NEGF-based model. One thing to note is that we are capturing the effect of large unetched regions at two ends with Σ_L and Σ_R. Since these are acting as spin-flip conductances we believe that etching out these regions would have significantly improved the spin signals.[58]

APPENDIX B: DERIVATION OF EQS. (5a) AND (5b)

We start by writing the incident state $\{\psi_i\}$ with a linear combination of $\{\psi_+\}$ and $\{\psi_-\}$

$$\{\psi_i\} = A\{\psi_+\} + B\{\psi_-\} = [\Psi]\begin{Bmatrix} A \\ B \end{Bmatrix}, \tag{B1}$$

where $[\Psi] \equiv [\{\psi_+\}\{\psi_-\}]$. After propagating from $x = 0$ to $x = L$, the final state is written as ($\theta_{+(-)} = k_{X+(-)}L$)

$$\begin{aligned}\langle\psi_f\rangle &= A\exp(i\theta_+)\{\psi_+\} + B\exp(i\theta_-)\{\psi_-\} \\ &= [\Psi]\begin{bmatrix} \exp(i\theta_+) & 0 \\ 0 & \exp(i\theta_-) \end{bmatrix}\begin{Bmatrix} A \\ B \end{Bmatrix}.\end{aligned} \tag{B2}$$

Hence we can write, $\{\psi_f\} = [t]\{\psi_i\}$, with

$$[t] = [\Psi]\begin{bmatrix} \exp(i\theta_+) & 0 \\ 0 & \exp(i\theta_-) \end{bmatrix}[\Psi]^{-1}, \tag{B3}$$

where

$$[\Psi] = \frac{1}{\sqrt{2}}\begin{bmatrix} 1 & 1 \\ \exp(i\phi_+) & -\exp(i\phi_-) \end{bmatrix}. \tag{B4}$$

Multiplying out the matrices leads to

$$[t] \equiv \frac{\begin{bmatrix} \exp(i\phi_+ + i\theta_-) + \exp(i\phi_- + i\theta_+) & \exp(i\theta_+) - \exp(i\theta_-) \\ \{\exp(i\theta_+) - \exp(i\theta_-)\}\exp(i\phi_+ + i\phi_-) & \exp(i\phi_+ + i\theta_+) + \exp(i\phi_- + i\theta_-) \end{bmatrix}}{\exp(i\phi_+) + \exp(i\phi_-)}. \tag{B5}$$

Setting $\phi_+ \approx \phi_- \equiv \phi$ (this amounts to ignoring the nonorthogonality of the + and − states), the expression simplifies to

$$[t] \equiv \frac{\begin{bmatrix} \exp(i\theta_+) + \exp(i\theta_-) & \{\exp(i\theta_+) - \exp(i\theta_-)\}\exp(-i\phi) \\ \{\exp(i\theta_+) - \exp(i\theta_-)\}\exp(i\phi) & \exp(i\theta_+) + \exp(i\theta_-) \end{bmatrix}}{2}. \tag{B6}$$

Note that $[t]$ can also be written as

$$[t] = \exp[i(\theta_+ + \theta_-)/2]\ \exp(i[\vec{\sigma}\cdot\hat{n}]\Delta\theta/2), \tag{B7}$$

where $\Delta\theta \equiv \theta_+ - \theta_- = \theta_L/\sqrt{1-s^2}$ and $\hat{n}$ is a unit vector in the direction of the effective magnetic field: $\hat{n} = \cos\phi\hat{x} + \sin\phi\hat{y}$. This form is intuitively appealing, showing the transmission $[t]$ as a product of a simple phase-shift $\exp\{i\,(\theta_+ + \theta_-)\,/2\}$ and a rotation around $\hat{n}$ by $\Delta\theta$. Also for the magnetic field applied along the z direction, which is in this case perpendicular to the x-y transport plane, giving rise to the Hanle effect (discussed in the paper earlier), the transmission function remains the same except that $\hat{n}$ now becomes $\hat{n} = \cos\phi\hat{x} + \sin\phi\hat{y} + \frac{g\mu_B B_z}{2\alpha k_0}\hat{z}$.

For z-polarized contacts in the parallel configuration,

$$\begin{aligned} t_{zz} &= \begin{Bmatrix} 1 & 0 \end{Bmatrix}[t]\begin{Bmatrix} 1 \\ 0 \end{Bmatrix} = t_{11}, \\ T_{zz} &= |t_{11}|^2 \approx \frac{1 + \cos(\theta_+ - \theta_-)}{2}, \end{aligned} \tag{B8}$$

and in the antiparallel configuration,

$$t_{\bar{z}z} = \{0\ 1\}\,[t]\begin{Bmatrix}1\\0\end{Bmatrix} = t_{21},$$
$$T_{\bar{z}z} = |t_{21}|^2 \approx \frac{1-\cos(\theta_+-\theta_-)}{2}. \tag{B9}$$

For x-polarized contacts in the parallel configuration,

$$t_{xx} = \frac{1}{2}\{1\ 1\}\,[t]\begin{Bmatrix}1\\1\end{Bmatrix} = \frac{t_{11}+t_{22}+t_{12}+t_{21}}{2},$$
$$T_{xx} \sim \left|\frac{(1+\cos\phi)\exp(i\theta_+)+(1-\cos\phi)\exp(\theta_-)}{2}\right|^2$$
$$\sim \frac{(1+\cos^2\phi)+\sin^2\phi\cos(\theta_+-\theta_-)}{2}, \tag{B10}$$

and in the antiparallel configuration,

$$t_{\bar{x}x} = \frac{1}{2}\{1\ -1\}\,[t]\begin{Bmatrix}1\\1\end{Bmatrix} = \frac{t_{11}-t_{22}+t_{12}-t_{21}}{2},$$
$$T_{\bar{x}x} \sim \frac{(1-\cos^2\phi)-\sin^2\phi\cos(\theta_+-\theta_-)}{2}. \tag{B11}$$

For y-polarized contacts in the parallel configuration,

$$t_{yy} = \frac{1}{2}\{1\ -i\}\,[t]\begin{Bmatrix}1\\+i\end{Bmatrix} = \frac{t_{11}+t_{22}+i(t_{12}-t_{21})}{2},$$
$$T_{yy} \sim \left|\frac{(1+\sin\phi)\exp(i\theta_+)+(1-\sin\phi)\exp(i\theta_-)}{2}\right|^2$$
$$\sim \frac{(1+\sin^2\phi)+\cos^2\phi\cos(\theta_+-\theta_-)}{2}, \tag{B12}$$

and in the antiparallel configuration,

$$t_{\bar{y}y} = \frac{1}{2}\{1\ +i\}\,[t]\begin{Bmatrix}1\\+i\end{Bmatrix} = \frac{t_{11}-t_{22}+i(t_{12}+t_{21})}{2},$$
$$T_{\bar{y}y} \sim \frac{(1-\sin^2\phi)-\cos^2\phi\cos(\theta_+-\theta_-)}{2}. \tag{B13}$$

Noting that $\tan\phi \approx -k_X/k_Y$ and $k_0^2 \approx k_X^2 + k_Y^2$ we can write

$$\Delta V_Z \sim T_{zz} - T_{\bar{z}z} = C_0\cos\left(\frac{2m^*\alpha L}{\hbar^2}\frac{k_0}{\sqrt{k_0^2-k_Y^2}}\right),$$
$$\Delta V_X \sim T_{xx} - T_{\bar{x}x}$$
$$= C_0\left\{\frac{k_Y^2}{k_0^2}+\left(1-\frac{k_Y^2}{k_0^2}\right)\cos\left(\frac{2m^*\alpha L}{\hbar^2}\frac{k_0}{\sqrt{k_0^2-k_Y^2}}\right)\right\},$$
$$\Delta V_Y \sim T_{yy} - T_{\bar{y}y}$$
$$= C_0\left\{\left(1-\frac{k_Y^2}{k_0^2}\right)+\frac{k_Y^2}{k_0^2}\cos\left(\frac{2m^*\alpha L}{\hbar^2}\frac{k_0}{\sqrt{k_0^2-k_Y^2}}\right)\right\}. \tag{B14}$$

APPENDIX C: DERIVATION OF EQS. (7a) AND (7b)

From Eqs. (6) and (5a),

$$\Delta V_X = \frac{1}{\pi}\int_0^1 ds\, V_{X0}(s) = \frac{B}{\pi}\int_0^1 ds\, s^2$$
$$+\frac{B}{\pi}\mathrm{Re}\left\{\int_0^1 ds\,(1-s^2)\exp\left(\frac{i\theta_L}{\sqrt{1-s^2}}\right)\right\}.$$

Noting that the phase has a stationary point at $s = 0$,[25] we expand it in Taylor's series around $s = 0$ to obtain

$$\Delta V_X \simeq \frac{C_0}{3\pi}$$
$$+\frac{C_0}{\pi}\mathrm{Re}\left[\int_0^{0+\epsilon} ds\,(1-s^2)\exp\left\{i\theta_L\left(1+\frac{s^2}{2}\right)\right\}\right]$$
$$\simeq \frac{C_0}{3\pi}+\frac{C_0}{\pi}\mathrm{Re}\left\{\exp(i\theta_L)\int_0^\infty ds\,\exp\left(i\theta_L\frac{s^2}{2}\right)\right\}$$
$$= \frac{C_0}{3\pi}+\frac{C_0}{\pi}\mathrm{Re}\left\{\exp(i\theta_L)\frac{\exp\left(i\frac{\pi}{4}\right)}{\sqrt{2\theta_L}}\Gamma\left(\frac{1}{2}\right)\right\}$$
$$= \frac{C_0}{3\pi}+\frac{C_0}{\sqrt{2\pi\theta_L}}\cos\left(\theta_L+\frac{\pi}{4}\right),$$

as stated in Eq. (7a).

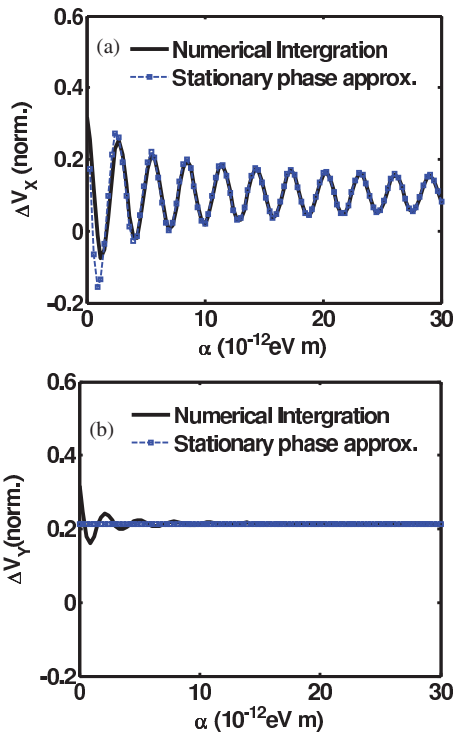

FIG. 10. (Color online) (a) Numerical calculation (squares) of Eqs. (6) and (5a) vs analytical expression (solid) in Eq. (7a) as a function of α. (b) Numerical calculation (squares) of Eqs. (6) and (5b) vs analytical expression (solid) in Eq. (7b), as a function of α.

Similarly from Eqs. (6) and (5b),

$$\Delta V_Y = \frac{C_0}{\pi}\int_0^1 ds\,(1-s^2) + \frac{C_0}{\pi}\mathrm{Re}\left\{\int_0^1 ds\,s^2 \exp\left(\frac{i\theta_L}{\sqrt{1-s^2}}\right)\right\} \simeq \frac{2C_0}{3\pi},$$

as stated in Eq. (7b). In Fig. 10 we compare stationary phase approximation with direct numerical integration.

APPENDIX D: SPIN COHERENCE OF HIGHER MODES

To include the effect of a finite spin-coherence length, we first express our mode-space expressions for spin voltages [Eqs. (6)] in real space. The mode-space variables can be mapped onto the real space [see Fig. 11(a)] in the following way:

$$s = \frac{k_Y}{k_0} = \sin\theta = \frac{y}{R},$$
$$\Delta V_X = \int_{-\infty}^{+\infty} dy \left\{\frac{y^2}{R^2} + \frac{L^2}{R^2}\cos\left(\frac{2m^*\alpha R}{\hbar^2}\right)\right\}\frac{L^2}{R^3},$$
$$\Delta V_Y = \int_{-\infty}^{+\infty} dy \left\{\frac{L^2}{R^2} + \frac{y^2}{R^2}\cos\left(\frac{2m^*\alpha R}{\hbar^2}\right)\right\}\frac{L^2}{R^3}. \quad \text{(D1)}$$

In Fig. 11(b) we see that the real-space expressions in Eqs. (D1) are in exact agreement with the mode-space expression in Eqs. (6).

From Fig. 11(a) we also realize that higher k_Y will travel a larger length $[R(k_Y) > R(k_Y = 0) = L]$ in the channel to reach the detecting contact. So a finite spin-coherence length λ_{sf} should gradually suppress the contribution from higher k_Y in $\Delta V_{X,Y}$. Including an exponential decay term representing the suppression of higher k_Y with λ_{sf}, Eqs. (D1) can be rewritten as

$$\Delta V_X = \int_{-\infty}^{+\infty} dy \left\{\frac{y^2}{R^2} + \frac{L^2}{R^2}\cos\left(\frac{2m^*\alpha R}{\hbar^2}\right)\right\} \times \frac{L^2}{R^3}\exp\left(\frac{-L}{\lambda_{sf}}\right),$$
$$\Delta V_Y = \int_{-\infty}^{+\infty} dy \left\{\frac{L^2}{R^2} + \frac{y^2}{R^2}\cos\left(\frac{2m^*\alpha R}{\hbar^2}\right)\right\} \times \frac{L^2}{R^3}\exp\left(\frac{-L}{\lambda_{sf}}\right). \quad \text{(D2)}$$

In Fig. 12 we see that spin voltages are reduced in amplitude as λ_{sf} reduces from a value of $\lambda_{sf} = 2\ \mu$m reported in the experiment[9] to a value of $\lambda_{sf} = 0.5\ \mu$m. But in addition we note that the ratio $\Delta V_Y/\Delta V_X$(p-p) is reduced from its point-contact limit in the shorter λ_{sf} case. To clarify the latter we show $\Delta V_Y(\lambda_{sf} = 0.5\ \mu\text{m})$ scaled up in amplitude to the value at $\Delta V_Y(\lambda_{sf} = 2\ \mu\text{m})$ within the experimental limit $\sim (8\text{–}13) \times 10^{-12}$ eV m by multiplying both ΔV_Y and $V_{X,P} = \Delta V_X/2$ for $\lambda_{sf} = 0.5\ \mu$m with the factor $f = \frac{\Delta V_Y(\lambda_{sf}=2\ \mu\text{m})}{\Delta V_Y(\lambda_{sf}=0.5\ \mu\text{m})}$ [see Fig. 12(b)]. However, from Fig. 12(b) we also realize that to make $\Delta V_Y \approx V_{X,P}$(p-p) we need λ_{sf} to be much smaller compared to the value mentioned in the experiment.[9]

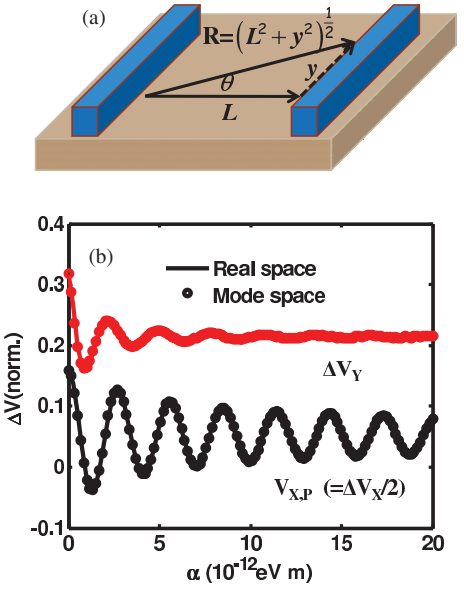

FIG. 11. (Color online) (a) Spin transport in real space where electrons of certain spin at higher k_Y mode travels a distance R at an angle θ which is greater than the distance L they travel at mode $k_Y = 0$. (b) Spin voltages ΔV_X and ΔV_Y from Eqs. (D1) (solid and dashed) and (6) (circles). Parameters are same as in Fig. 2.

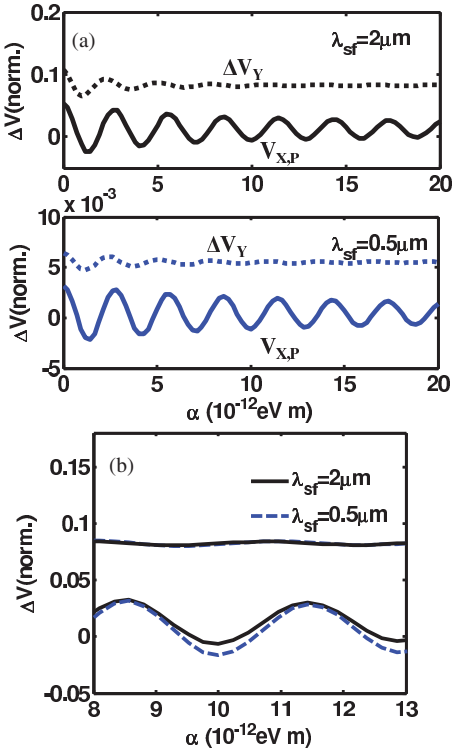

FIG. 12. (Color online) (a) Spin voltages ΔV_Y and $V_{X,P} = \Delta V_X/2$ at different spin-coherence length λ_{sf}, (b) same voltages in (a) plotted within the experimental range of α in Ref. 9, and for the purpose of comparison, in all cases ΔV_Y at different λ_{sf} is scaled up in amplitude to the value at $\lambda_{sf} = 2\ \mu$m and accordingly ΔV_X are multiplied with the same scaling factors, respectively.

APPENDIX E: SPIN CURRENT

To obtain the spin current at a given terminal, we used the current operator described in Ref. 53 (see Eq. 8.6.5, p. 317). The expression for spin-current density at any grid point can be written as

$$\vec{I}_s(k_y) = \mathrm{Re}\big(\mathrm{Tr}(i\vec{\sigma}[G(k_y)\Sigma^{in}(k_y) - \Sigma^{in}(k_y)G^{\dagger}(k_y) - \Sigma_i(k_y)G^n(k_y) + G^n(k_y)\Sigma_i^{\dagger}(k_y)])\big). \quad \text{(E1)}$$

Here, $\vec{\sigma}$ is the Pauli spin matrix, Σ^{in} is the in-scattering function, G is Green's function, $G^n(\equiv -iG^<)$ is the correlation function whose diagonal elements are electron density, and Σ_i is the contact self-energy ($i = 1, 2, 3, 4$). Equation (E1) is integrated over all the transverse modes (k_y) to obtain the total spin current at any energy. In Fig. 13 we compare the spin-current ($I_{s,0}$) from Eqn. (E1) with the expression $I_{s,0} = \frac{\Delta V_0}{P_C}\frac{2G_MG_m}{G_M+G_m}$ at $\alpha = 0$ and a good agreement is found. Here, I_s increases with the interfacial conductance of the magnet for a given spin-polarization and charge current.

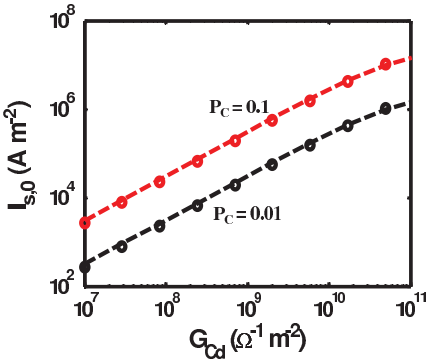

FIG. 13. (Color online) Comparison of spin-current flowing into the detecting magnet in Fig. 1 calculated from NEGF equation (circles) against the same obtained from the equivalent circuit model (solid) in Appendix A, as a function of detecting contact conductance $G_{Cd} = (G_M + G_m)$ and P_C. Parameters: $L_{Ci} = 0.2\ \mu$m, $L_{Cd} = 0.25\ \mu$m. Injecting magnet's contact conductance is fixed at $G_{Ci} = 4 \times 10^{10}\ \Omega^{-1}\mathrm{m}^{-2}$ and charge current of 1 mA is maintained all through out. Carrier density $n_S = 2.7 \times 10^{12}\ \mathrm{cm}^{-2}$.

*azainudd@purdue.edu
†datta@purdue.edu

[1] S. Datta and B. Das, Appl. Phys. Lett. **56**, 665 (1990).
[2] Yu. A. Bychkov and E. I. Rashba, JETP Lett. **39**, 78 (1984).
[3] J. Nitta, T. Akazaki, H. Takayanagi, and T. Enoki, Phys. Rev. Lett. **78**, 1335 (1997).
[4] G. Schmidt, J. Phys. D: Appl. Phys. **38**, R107 (2005).
[5] E. I. Rashba, Phys. Rev. B **62**, R16267 (2000).
[6] A. Fert and H. Jaffres, Phys. Rev. B **64**, 184420 (2001).
[7] D. L. Smith and R. N. Silver, Phys. Rev. B **64**, 045323 (2001).
[8] G. E. W. Bauer, Y. Tserkovnyak, A. Brataas, J. Ren, K. Xia, M. Zwierzycki, and P. J. Kelly, Phys. Rev. B **72**, 155304 (2005).
[9] H. C. Koo, J. H. Kwon, J. Eom, J. Chang, S. H. Han, and M. Johnson, Science **325**, 1515 (2009).
[10] See, for example, M. Johnson and R. H. Silsbee, Phys. Rev. B **37**, 5312 (1988); F. J. Jedema, M. S. Nijboer, A. T. Filip, and B. J. van Wees, *ibid.* **67**, 085319 (2003).
[11] T. P. Pareek and P. Bruno, Phys. Rev. B **65**, 241305 (2002).
[12] M. Governale and U. Zülicke, Solid State Commun. **131**, 581 (2004).
[13] B. K. Nikolić and S. Souma, Phys. Rev. B **71**, 195328 (2005).
[14] J. S. Jeong and H. W. Lee, Phys. Rev. B **74**, 195311 (2006).
[15] M.-H. Liu and C.-R. Chang, Phys. Rev. B **73**, 205301 (2006).
[16] M. M. Gelabert, L. Serra, D. Sanchez, and R. Lopez, Phys. Rev. B **81**, 165317 (2010).
[17] M. G. Pala, M. Governale, J. König, and U. Zülicke, Europhys. Lett. **65**, 850 (2004).
[18] P. Agnihotri and S. Bandyopadhyay, Physica E **42**, 1736 (2010).
[19] See, for example, S. A. Wolf, D. D. Awschalom, R. A. Buhrman, S. von. Molnár, M. L. Roukes, A. Y. Chtchelkanova, and D. M. Treger, Science **294**, 1488 (2001); S. Bandyopadhyay, Phys. Rev. B **61**, 13813 (2000); S. D. Sarma, J. Fabian, X. Hu, and I. Zutic, Solid State Commun. **119**, 207 (2001).
[20] S. Takahashi and S. Maekawa, Phys. Rev. B **67**, 052409 (2003).
[21] S. Datta, in *Oxford Handbook on Nanoscience and Nanotechnology*, edited by A. V. Narlikar and Y. Y. Fu (Oxford University, Oxford, 2010), Vol. 1, Chap. 1, also available in e-print arXiv:0809.4460v2.
[22] M. Johnson and R. H. Silsbee, Phys. Rev. Lett. **55**, 1790 (1985).
[23] A. Fert, J.-M. George, H. Jaffres, and R. Mattana, IEEE Trans. Electron Devices **54**, 921 (2007).
[24] S. Datta, *Quantum Transport: Atom to Transistor* (Cambridge University, Cambridge, England, 2005).
[25] N. Bleistein and R. Handelsman, *Asymptotic Expansions of Integrals* (Dover, New York, 1986); Jon Mathews and L. Robert. *Mathematical Methods of Physics*, 2nd ed. (Benjamin, New York, 1970).
[26] J. Luo, H. Munekata, F. F. Fang, and P. J. Stiles, Phys. Rev. B **41**, 7685 (1990).
[27] T. Koga, J. Nitta, T. Akazaki, and H. Takayanagi, Phys. Rev. Lett. **89**, 046801 (2002).
[28] S. D. Ganichev, V. V. Bel'kov, L. E. Golub, E. L. Ivchenko, P. Schneider, S. Giglberger, J. Eroms, J. De Boeck, G. Borghs, W. Wegscheider, D. Weiss, and W. Prettl, Phys. Rev. Lett. **92**, 256601 (2004).
[29] S. Giglberger, L. E. Golub, V. V. Bel'kov, S. N. Danilov, D. Schuh, C. Gerl, F. Rohlfing, J. Stahl, W. Wegscheider, D. Weiss, W. Prettl, and S. D. Ganichev, Phys. Rev. B **75**, 035327 (2007).
[30] A. Łusakowski, J. Wróbel, and T. Dietl, Phys. Rev. B **68**, 081201(R) (2003).
[31] M. I. D'yakonov and V. I. Perel, Sov. Phys. JETP **33**, 1053 (1971).
[32] M. I. D'yakonov and V. I. Perel, Sov. Phys. Solid State **13**, 3023 (1972).
[33] S. Pramanik, S. Bandyopadhyay, and M. Cahay, Phys. Rev. B **68**, 075313 (2003).
[34] A. Khaetskii, Phys. Rev. Lett. **96**, 056602 (2006).
[35] L. Hu, Z. Huang, and S. Hu, Phys. Rev. B **73**, 235314 (2006).

[36]T. Valet and A. Fert, Phys. Rev. B **48**, 7099 (1993).
[37]H. C. Koo. H. Yi, J.-B. Ko, J. Chang, S.-H. Han, D. Jung, S.-G. Huh, and J. Eom, Appl. Phys. Lett. **90**, 022101 (2007).
[38]K.-H. Kim, H.-J. Kim, H. C. Koo, J. Chang, and S.-H. Han, Appl. Phys. Lett. **97**, 012504 (2010).
[39]J. D. Koralek, C. P. Weber, J. Orenstein, B. A. Bernevig, S.-C. Zhang, S. Mack. and D. D. Awschalom, Nature (London) **458**, 610 (2009).
[40]J. Eroms, M. Tolkiehn, D. Weiss, U. Rössler, J. D. Boeck, and G. Borghs, Europhys. Lett. **58**, 569 (2002).
[41]J. Z. Sun, Phys. Rev. B **62**, 570 (2000).
[42]J. Slonczewski, J. Magn. Magn. Mater. **159**, L1 (1996).
[43]L. Berger, Phys. Rev. B **54**, 9353 (1996).
[44]T. Yang, T. Kimura, and Y. Otani, Nature Phys. **4**, 851 (2008).
[45]J. Z. Sun, M. C. Gaidis, E. J. O'Sullivan, E. A. Joseph, G. Hu, D. W. Abraham, J. J. Nowak, P. L. Trouilloud, Yu Lu, S. L. Brown, D. C. Worledge, and W. J. Gallagher, Appl. Phys. Lett. **95**, 083506 (2009).
[46]D. Chiba, Y. Sato, T. Kita, F. Matsukura, and H. Ohno, Phys. Rev. Lett. **93**, 216602 (2004).
[47]M. Elsen, O. Boulle, J.-M. George, H. Jaffrs, R. Mattana, V. Cros, A. Fert, A. Lemaitre, R. Giraud, and G. Faini, Phys. Rev. B **73**, 035303 (2006).
[48]A. Manchon and S. Zhang, Phys. Rev. B **78**, 212405 (2008).
[49]K. M. D. Hals, A. Brataas, and Y. Tserkovnyak, Europhys. Lett. **90**, 47002 (2010).
[50]P. M. Haney and M. D. Stiles, Phys. Rev. Lett. **105**, 126602 (2010).
[51]A. Chernyshov, M. Overby, X. Liu, J. K. Furdyna, Y. L. Geller, and L. P. Rokhinson, Nature Phys. **5**, 656 (2009).
[52]I. M. Miron, G. Gaudin, S. Auffret, B. Rodmacq, A. Schuhl, S. Pizzini, J. Vogel, and P. Gambardella, Nat. Mater. **9**, 230 (2010).
[53]S. Datta, *Electronic Transport in Mesoscopic Systems* (Cambridge University, Cambridge, England, 1997).
[54]C. H. Benett, Int. J. Theor. Phys. **21**, 905 (1982).
[55]K. K. Likharev and A. N. Korotkov, Science **273**, 763 (1996).
[56]B. Behin-Aein, D. Datta, S. Salahuddin, and S. Datta, Nature Nanotech. **5**, 266 (2010).
[57]W. F. Brown, IEEE Trans. Magn. **15**, 1196 (1979).
[58]A. N. M. Zainuddin, H. Kum, D. Basu, S. Srinivasan, L. Siddiqui, P. Bhattacharya, and S. Datta, J. Appl. Phys. **108**, 123913 (2010).